Supplementary Online Materials

Pokrovski et al.

Gold speciation in hydrothermal fluids revealed by in situ high energy resolution X-ray absorption spectroscopy

This file contains:

-Supplementary Text,

-Supplementary Tables OM1 and OM2,

-Supplementary Figures OM1 to OM4,

-Supplementary References

SUPPLEMENTARY TEXT

Determination of Au dissolved concentration from XAS spectra

Dissolved gold concentrations were determined from the amplitude of the absorption edge height of Au L_3-edge spectra independently in transmission and fluorescence modes (Table OM1).

The edge step of the transmission spectra ($\Delta\mu_{tr}$) was converted to Au concentration using the classical X-ray absorption relation based on the Beer-Lamber law (see Pokrovski et al. 2005, 2006, 2008 for details):

$$m_{Au}(\mathrm{tr}) = \Delta\mu_{tr} / (\Delta\sigma_{Au} \times M_{Au} \times l_{path} \times d_{fluid}) \quad \text{(S1)}$$

where m_{Au} is the Au aqueous concentration (mol/kg of fluid), $\Delta\sigma_{Au}$ is the change of the total absorption cross-section of Au over its L_3-edge (111.195 cm^2/g; Elam et al. 2002), l_{path} is the optical path length inside the cell (cm) which remains constant through the experiment, M_{Au} is Au atomic weight (0.197 kg/mol), and d_{fluid} is the fluid density (g/cm^3) at given *T-P*. In the absence of direct volumetric data on the system H_2O-$K_2S_2O_3$-KOH-HCl-Au at elevated *T-P*, the fluid density was approximated using the Pressure-Volume-Temperature-Composition (*PVTX*) properties of the system NaCl-H_2O (Driesner and Heinrich 2007), and assuming that addition of each corresponding solute to pure water yields the same contribution to the fluid density as the addition of equivalent weight concentration of NaCl. The maximal error from this approximation does not exceed 10% of the total d_{fluid} value at experimental *T-P* (Pokrovski et al. 2009a). The height of the absorption-edge step ($\Delta\mu_{tr}$) in each transmission scan was determined using the AUTOBK algorithm implemented in the Athena software (Ravel and Newville 2005), which yields uncertainties typically ranging from <5% at $\Delta\mu_{tr}$ >0.1 to 50% at $\Delta\mu_{tr}$ <0.01 (see Pokrovski et al. 2005, 2006 for more details). The optical path length was determined from the exact cell position versus the beam path and using the circular geometry of the glassy-carbon tube (±0.005 cm). The overall error-propagated uncertainty (±2 s.d.) of Au concentration determination is ~50% of the absolute value in our experiments.

A complementary approach for estimating Au concentration is using the edge-step in fluorescence mode ($\Delta\mu_{fl}$), which is much greater in amplitude than $\Delta\mu_{tr}$, but requires Au concentration standards with similar or close matrix absorbance as the experimental fluid:

$$m_{Au}^{exp}(\mathrm{fl}) = (\Delta\mu_{fl}^{exp} / \Delta\mu_{fl}^{st}) \times (A_{fluid}^{exp} / A_{fluid}^{st}) \times (d_{fluid}^{st} / d_{fluid}^{exp}) \times m_{Au}^{st} \quad \text{(S2)}$$

where exp and st stand for the experimental and standard Au solution, respectively, m_{Au} is the Au concentration in the fluid (mol/kg), d_{fluid} is the fluid density, and A_{fluid} is the fluid total absorbance which is estimated as

$$A_{fluid} = \sum_i (m_i \times \sigma_i \times M_i) \times l_{path} \times d_{fluid} \quad \text{(S3)}$$

where m_i is the concentration (mol/kg of fluid) of i-th component of the fluid phase (i = O, H, Au, Na or S), σ_i is its absorption cross-section at a given energy (cm^2/g), M_i is its atomic weight (kg/mol), l_{path} is the optical path length inside the cell (cm), and d_{fluid} is the fluid density (g/cm^3) at given *T-P*. As the standard Au solution, we used a 0.00503*m* $HAuCl_4$ in an HCl-NaCl matrix (prepared gravimetrically, Table OM1) whose absorbance was close as possible to that of the experimental fluids to preserve the proportionality in equation (S2). Being unstable at elevated temperatures (Pokrovski et al. 2009b), this auric chloride solution was measured both in transmission and fluorescence modes at 20°C and 1 bar in the same optical cell geometry as the two experimental solutions at high *T-P*. Considering potential uncertainties related to such calibration and absorption corrections, a reasonable overall error in Au concentration estimation from the fluorescence signal is 50% of the value (±2 s.d.).

Dissolved Au concentrations determined from scans in transmission and fluorescence modes as a function of time elapsed from the moment of attainment of the experimental temperature are shown in

Fig. OM1. Although the values of fluorescence-derived Au concentrations in both experiments are somewhat higher than their transmission-derived counterparts, their associated uncertainties overlap. These uncertainties stem from different sources. The transmission-edge step is more direct to interpret, but is affected by larger errors intrinsic to small Au concentrations (<0.001–0.01*m* Au; see Pokrovski et al. 2005 for more detailed discussions). The fluorescence-edge step value, by contrast, is far greater and thus more accurately measurable, but its conversion to absolute Au concentration is strongly dependent on the overall matrix absorption, which is difficult to accurately quantify in the absence of standards measured at the experimental *T*-*P*-composition parameters. Therefore, considering these caveats, no preference could be given to one or the other data source, and the mean value for Au concentration derived from transmission and fluorescence data would be the most plausible one and was thus used in the further interpretation.

The mean Au concentrations for each scan in experiment 1 display a slight decrease with time, which may be due to i) minor sulfur loss from the fluid owing to its partial precipitation in the colder parts of the optical cell (e.g., Pokrovski et al. 2009a), and/or ii) kinetic evolution of sulfur ligand concentrations following thiosulfate breakdown and re-equilibration among the produced species (reactions 3 and 4 in the main text) that typically require a few hours at these *T* and pH conditions to reach complete chemical equilibrium (e.g., Pokrovski and Dubessy 2015; Kokh et al. 2020). Only two scans could be measured for experiment 2 within the period from 8 to 9 hours elapsed after the temperature attainment (due to the failure of an alignment motor). Nevertheless, they show similar within errors edge-step values, and the elapsed time was sufficiently long to ensure the attainment of equilibrium.

First-principles molecular dynamics (FPMD) simulations

Details on FPMD simulations were given in Pokrovski et al. (2015) and are thus only briefly summarized here. We used the CP2K code package (VandeVondele et al. 2005) in the framework of the density functional theory (DFT) as implemented in the QUICKSTEP module, with the BLYP exchange-correlation functional (Becke 1988; Lee et al. 1988) in combination with a van der Waals correction DFT-D3 (Grimme et al. 2010). A plane-wave cutoff of 600 Ry for the electronic density and a triple-zeta valence doubly polarizable (TZV2P) basis set were chosen for all elements except Au, which was described by means of a double-zeta valence polarizable (DZVP) basis set optimized for molecular geometries (VandeVondele and Hutter 2007). The interaction between the ionic cores and the valence electrons was treated with pseudo-potentials (Goedecker et al. 1996). In systems with an odd number of electrons (such as with the $S_3^{\bullet-}$ ion) spin polarization was taken into account. The Born-Oppenheimer molecular dynamics simulations were carried out in the *NVT* ensemble with a time step of 0.5 fs, and the system was thermostated at 400°C by means of a stochastic velocity rescaling algorithm (Bussi et al. 2007) with a time constant of 1 ps. The solvent density was fixed to 0.7 g/cm^3, which corresponds to a pressure of ~600 bar for heavy water at 400°C, which is close to the experimental fluid density of the present study (0.8 g/cm^3). The cubic simulation box contained at least 126 water molecules, and periodic boundary conditions were applied. Some water molecules were then replaced by different Au-S complexes, assuming equal partial molar volumes for S, HS^- and H_2O and neglecting the partial molar volume of Au^+. For hydrogen, the mass of the heavy isotope deuterium was chosen, which allows a larger time step for the integration of the equation of motion without affecting significantly the chemistry of bonding. Simulations from 10 to 50 ps duration time were used to estimate the stability of different Au-S species and to extract a few significant structures of different Au-S species that were used then as input for FDMNES-XANES spectra calculations.

This extraction employed the *k*-means method (Hartigan and Wong 1979), which consists in partitioning the configurations into several groups or clusters based on the condition that the average interatomic distance difference among the configurations and the barycenter of the cluster should be minimum. As the quantitative criterion of the distance difference between two atomic configurations, the Root Mean Square Deviation (RMSD) between atomic positions has been adopted. After some trial and errors, we chose to perform *k*-means clustering of 100 configurations into 6 clusters for each Au complex. While the barycenter of atomic configurations of each cluster represents an average configuration, it turns out that they are not directly appropriate for XANES spectra calculations because interatomic distances are not typical of the true configurations encountered in the FPMD simulations. This is the result of a non-linear transformation between Cartesian coordinates and interatomic distances. Therefore, we have chosen instead to extract actual FPMD configurations typical of each cluster. This extraction was performed by selecting, within each cluster, a single typical FPMD configuration whose ensemble of interatomic distances minimally differs from those of all other configurations within the same cluster.

SUPPLEMENTARY TABLES

Supplementary Table OM1. Au L_3 absorption edge transmission (tr) and fluorescence (fl) signals and the corresponding Au aqueous concentration in individual scans as a function of time elapsed from the attainment of the run temperature in the two experiments at 350°C and 600 bar performed in this study.

duration (h)	$\Delta\mu_{tr}$	m_{Au} (tr) (mol/kg fluid) [b]	$\Delta\mu_{fl}$	A_{fluid}	m_{Au} (fl) (mol/kg fluid) [b]	m_{Au} mean fl-tr [c]
Standard: 0.00503(±0.00003)m $HAuCl_4$ + 0.454m KCl + 0.409m HCl, d_{fluid}=1.033 g/cm^3, l_{path}=0.333 cm						
0.5	0.0379	0.00503[a]	35.86	1.754	0.00503[a]	
Exp 1: 0.46m $K_2S_2O_3$ + 0.20m HCl, d_{fluid}=0.81 g/cm^3, l_{path}=0.357 cm						
0.42	0.0159	0.0025	38.39	1.796	0.00704	
0.79	0.0160	0.0025	34.57	1.780	0.00628	
1.17	0.0145	0.0023	32.82	1.765	0.00591	
1.69	0.0124	0.0020	28.70	1.741	0.00510	
2.50	0.0114	0.0018	24.61	1.718	0.00432	
mean Au		*0.0022*			*0.0057*	**0.004 ± 0.002**
exp 2: 0.51m $K_2S_2O_3$ + 0.29m KOH, d_{fluid}=0.825 g/cm^3, l_{path}=0.346 cm						
8.03	0.0267	0.00426	57.42	1.876	0.01078	
8.44	0.0232	0.00371	54.61	1.871	0.01023	
mean Au		*0.0040*			*0.0105*	**0.007 ± 0.004**
error (2σ)		50%			50%	

[a] Known Au concentration, accurately prepared by weight, by dissolving a piece of gold (99.99%) in aqua regia.
[b] See equations (S1) to (S3).
[c] Values in bold = mean of the average fluorescence and transmission data; error = estimated standard deviation at 2σ probability level (≈ ±2 s.d.).

Supplementary Table OM2. Gold-ligand (SH, S_3, Cl, OH_2) interatomic distances (in Å) predicted in this study by static DFT calculations using the indicated exchange-correlation functionals and by FPMD (average values over the whole set of 100 snapshots per species), and their comparison with experimental EXAFS-fitted values.

species	Au-ligand	B3LYP	PBE0	BLYP	PBE	FPMD	EXAFS
$Au(HS)_2^-$	Au-SH	2.336	2.303	2.353	2.313	2.414	2.290 ± 0.005[a]
$Au(HS)S_3^-$	Au-SH	2.321	2.290	2.339	2.301	2.395	2.290 ± 0.005[a]
	Au-S_3	2.323	2.290	2.328	2.289	2.399	
$Au(HS)H_2O^0$	Au-SH	2.250	2.225	2.263	2.232	2.333	-
	Au-OH_2	2.225	2.183	2.257	2.212	2.287	
$Au(S_3)_2^-$	Au-S_3	2.315	2.285	2.325	2.287	2.389	-
$AuCl_4^-$	Au-Cl	2.331	2.295	2.362	2.322	-	2.282 ± 0.004[b]

[a] EXAFS-derived Au-S distance from extensive normal-resolution measurements in gold-saturated $(K,Na)_2S_2O_3$-S-(K,Na)OH aqueous solutions from 200 to 450°C and 500-700 bar and reference Au(I) thiol compounds; no distinction could be made between Au-SH and Au-S_3 bonds (Pokrovski et al. 2015); errors = estimated standard deviation from fits of multiple spectra from different experiments.
[b] EXAFS-derived Au-Cl distance from normal-resolution measurements of $HAuCl_4$-HCl-NaCl aqueous solutions at 20-150°C and 600 bar (Pokrovski et al. 2009b).

SUPPLEMENTARY FIGURES

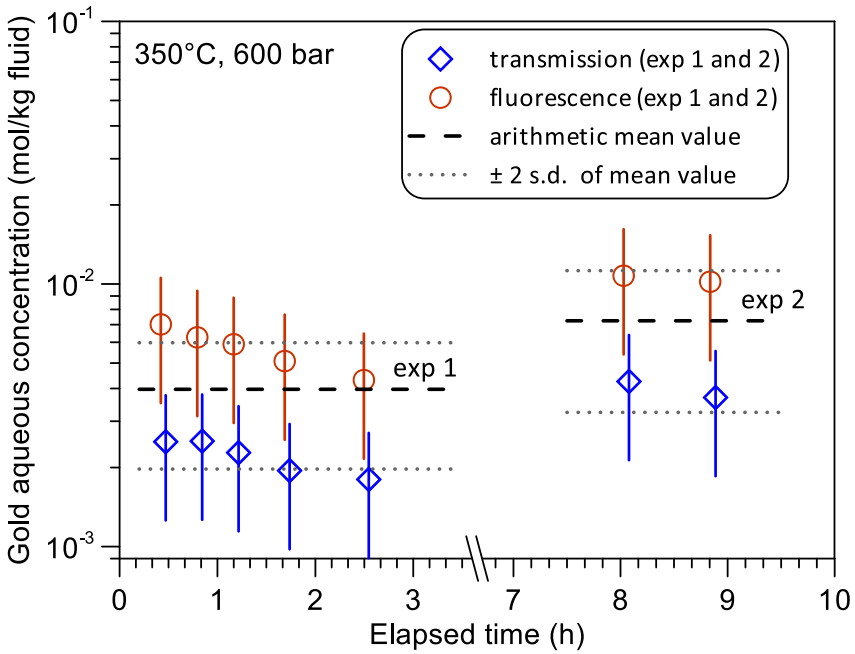

Supplementary Figure OM1. Evolution, as a function of time, of dissolved gold concentration in solution, determined from the absorption edge height in transmission and fluorescence modes in the two experiments of this study. The dashed horizontal lines stand for the average Au concentration value of the whole set of transmission and fluorescence data points for each experiment whereas the lower and upper dotted lines denote its corresponding standard error margins (±2 s.d. of the mean). Note that the transmission vs fluorescence datapoints were slightly shifted along the *x*-axis to allow better visualization of the associated error bars.

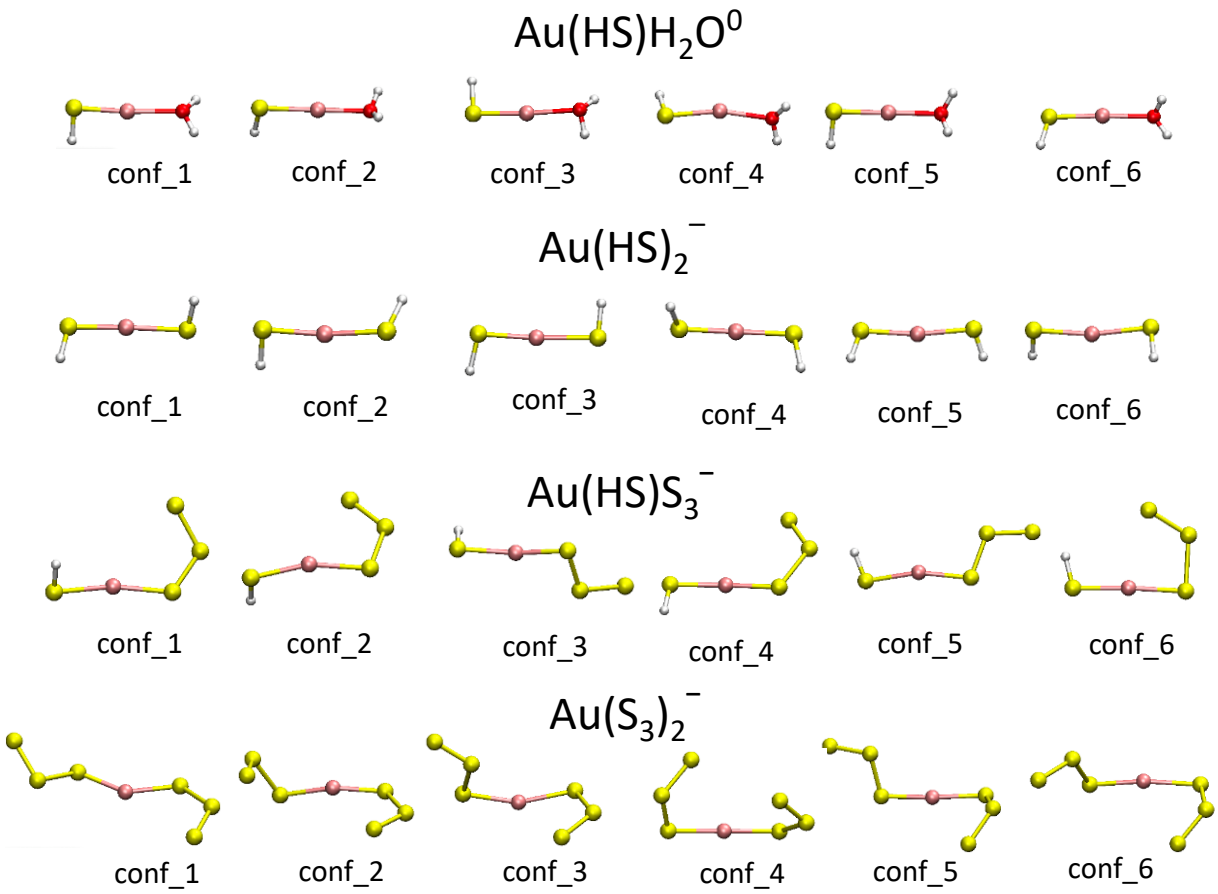

Supplementary Figure OM2. Structures of the indicated Au-complexes generated by FPMD simulations and extracted by using the clustering method described in the main text and used to simulate their XANES spectra using FDMNES (shown in Supplementary Figs OM3 and OM4).

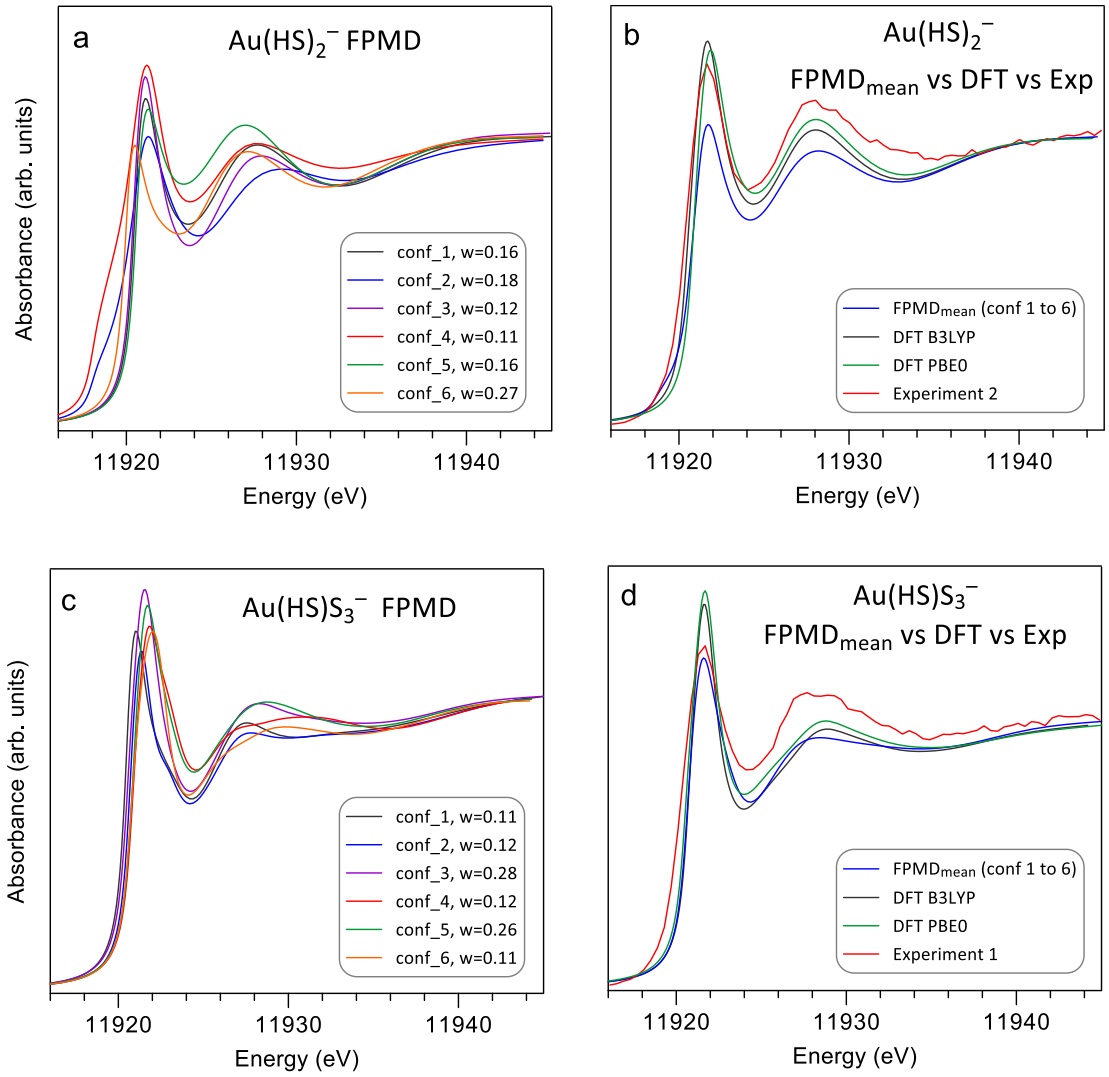

Supplementary Figure OM3. FDMNES-calculated Au L_3-edge XANES spectra of the $Au(HS)_2^-$ and $Au(HS)S_3^-$ complexes simulated by molecular dynamics (FPMD) and extracted using the clustering method (**a** and **c**), and the comparison of the mean FPMD spectrum with the spectra calculated using static DFT geometries and with experimental spectra (**b** and **d**). For each examined species, FPMD-generated geometric configurations were grouped in larger clusters based on their Root Mean Square Deviation (RMSD) of atomic positions, conf_1 to conf_6 with relative weights (w) corresponding to the number of individual configurations in each group (**a** and **c**). Then the average FPMD spectrum was calculated as the mean of the 6 spectra (**b** and **d**) and compared with spectra from configurations generated by static DFT with the indicated electronic functional (B3LYP and PBE0). It can be seen in (**b**) and (**d**) that the mean FPMD spectra of $Au(HS)_2^-$ and $Au(HS)S_3^-$ have shapes and energy positions very similar to those both from the corresponding experiment and static DFT calculations, attesting to the general validity of our approach. The slightly lower absolute amplitude of the white-line of the mean FPMD spectrum of both species compared to the experiment and static DFT may be owing to minor under-sampling by the *k*-means method using 6 clusters of the whole set of possible MD geometric configurations. These differences are expected to be eliminated in future work using a larger number of representative MD configurations.

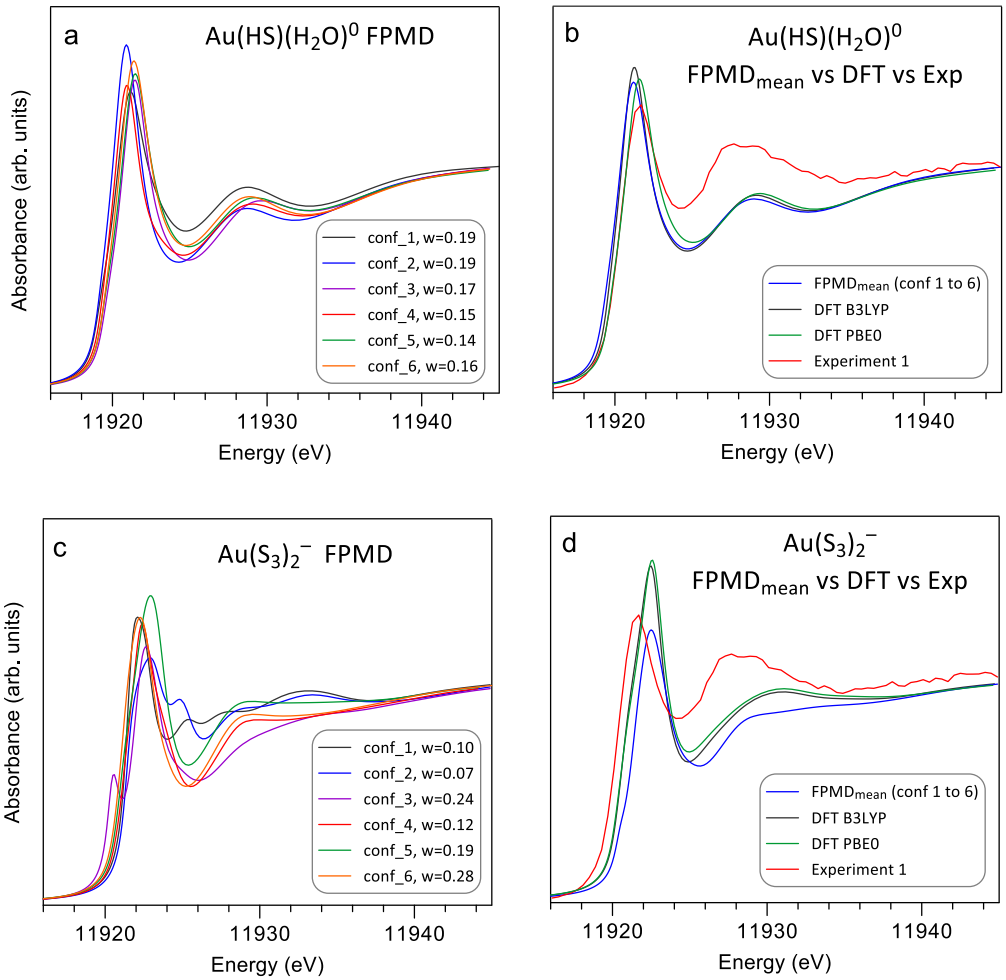

Supplementary Figure OM4. FDMNES-calculated Au L_3-edge XANES spectra of the $Au(HS)H_2O$ and $Au(S_3)_2^-$ complexes simulated by molecular dynamics (FPMD) and extracted using the clustering method (**a** and **c**), and the comparison of the mean FPMD spectra with those calculated using static DFT geometries and with experimental spectra (**b** and **d**). See the Fig. OM3 caption for details. It can be seen in (**b**) that the mean FPMD spectrum of $Au(HS)H_2O$ is very close to those from static DFT, but is significantly different from the experiment. The mean FPMD spectrum of $Au(S_3)_2^-$ has a lower-amplitude white line and a less expressed post-edge resonance compared to the DFT spectra (**d**), which is likely due to strongly changing dynamic geometry of the complex in FPMD simulations and/or insufficient statistics provided by 6 MD clusters for such a large complex. Nevertheless, the general shape and energy positions of the main features of the FPMD spectrum are similar to its DFT counterparts, supporting the validity of the simple static DFT approach for approximation of the species geometry and corresponding XANES spectra. Note that both FPMD and DFT spectra are different from the experimental one, confirming that the chosen species are likely to be negligible in the experimental fluid.

SUPPLEMENTARY REFERENCES

Becke, A.D. (1988) Density-functional exchange-energy approximation with correct asymptotic behavior. Physical Review A, 38, 3098–3100.

Bussi, G., Donadio, D., and Parrinello, M. (2007) Canonical sampling through velocity rescaling. The Journal of Chemical Physics, 126, 014101/1–7.

Driesner, T., and Heinrich, C.A. (2007) The system H_2O–NaCl. Part I: Correlation formulae for phase relations in temperature–pressure–composition space from 0 to 1000 °C, 0 to 5000 bar, and 0 to 1 X_{NaCl}. Geochimica et Cosmochimica Acta, 71, 4880–4901.

Elam, W.T., Ravel, B.D., and Sieber, J.R. (2002) A new atomic database for X-ray spectroscopic calculations. Radiation Physical Chemistry, 63, 121–128.

Goedecker, S., Teter, M., and Hutter, J. (1996) Separable dual-space Gaussian pseudopotentials. Physical Review B, 54, 1703–1710.

Grimme, S., Antony, J., Ehrlich, S., and Krieg, H. (2010) A consistent and accurate ab initio parameterization of density functional dispersion correction (DFTD) for the 94 elements H-Pu. The Journal of Chemical Physics, 132, 154104/1–19.

Hartigan, J.A., and Wong, M.A. (1979) A *k*-means clustering algorithm. Applied Statistics, 28, 100–108.

Kokh, M.A., Assayag, N., Mounic, S., Cartigny, P., Gurenko, A., and Pokrovski, G.S. (2020) Multiple sulfur isotope fractionation in hydrothermal systems in the presence of radical ions and molecular sulfur. Geochimica et Cosmochimica Acta, 285, 100–128.

Lee, C., Yang, W., and Parr, R.G. (1988) Development of the Colle-Salvetti correlation-energy formula into a functional of the electron density. Physical Review B, 37, 785–789.

Pokrovski, G.S., and Dubessy, J. (2015) Stability and abundance of the trisulfur radical ion S_3^- in hydrothermal fluids. Earth and Planetary Science Letters, 411, 298–309.

Pokrovski, G.S., Roux, J., Hazemann, J.-L., and Testemale, D. (2005) An X-ray absorption spectroscopy study of argutite solubility and germanium aqueous speciation in hydrothermal fluids to 500°C and 400 bar. Chemical Geology, 217, 127–145.

Pokrovski, G.S., Borisova, A.Y., Roux, J., Hazemann, J.-L., Petdang, A., Tella, M., and Testemale, D. (2006). Antimony speciation in saline hydrothermal fluids: A combined X-ray absorption fine structure and solubility study. Geochimica et Cosmochimica Acta, 70, 4196–4214.

Pokrovski, G.S., Roux, J., Hazemann, J.-L., Borisova, A.Y., Gonchar, A.A., and Lemeshko, M.P. (2008) In situ X-ray absorption spectroscopy measurement of vapor-brine fractionation of antimony at hydrothermal conditions. Mineralogical Magazine, 72, 667–681.

Pokrovski, G.S., Tagirov, B.R., Schott, J., Hazemann, J-L., and Proux, O. (2009a) A new view on gold speciation in sulfur-bearing hydrothermal fluids from in-situ X-ray absorption spectroscopy and quantum-chemical modeling. Geochimica et Cosmochimica Acta, 73, 5406–5427.

Pokrovski, G.S., Tagirov, B.R., Schott, J., Bazarkina, E.F., Hazemann, J.-L., and Proux, O. (2009b) An in situ X-ray absorption spectroscopy study of gold-chloride complexing in hydrothermal fluids. Chemical Geology, 259, 17–29.

Pokrovski, G.S., Kokh, M.A., Guillaume, D., Borisova, A.Y., Gisquet, P., Hazemann, J.-L., Lahera, E., Del Net, W., Proux, O., Testemale, D., Haigis, V., Jonchière, R., Seitsonen, A.P., Ferlat, G., Vuilleumier, R., Saitta, A.M., Boiron, M.-C., and Dubessy, J. (2015) Sulfur radical species form gold deposits on Earth. Proceedings of the National Academy of Sciences of the USA, 112, 13484–13489.

Ravel, B., and Newville, M. (2005) ATHENA, ARTEMIS, HEPHAESTUS: data analysis for X-ray absorption spectroscopy using IFEFFIT. Journal of Synchrotron Radiation, 12, 537–541.

VandeVondele, J., et al. (2005) Quickstep: fast and accurate density functional calculations using a mixed Gaussian and plane waves approach. Computer Physics Communications, 167, 103–128; http://www.cp2k.org.

VandeVondele, J., and Hutter, J. (2007) Gaussian basis sets for accurate calculations on molecular systems in gas and condensed phases. The Journal of Chemical Physics, 127, 114105.